SIMULATION OF POROSITY AND HOT TEARS IN A SQUEEZE CAST MAGNESIUM CONTROL ARM

K.D. Carlson[1], C. Beckermann[1], J. Jekl[2], R. Berkmortel[2]

[1]Department of Mechanical and Industrial Engineering, University of Iowa, Iowa City, IA 52242, USA
[2]Meridian Lightweight Technologies, Strathroy, Ontario, Canada

Keywords: Magnesium Alloys, Casting, Shrinkage Porosity, Hot Tears, Modeling

Abstract

Simulations are performed for the squeeze casting of AM60 and AZ91 automotive control arms. Advanced feeding flow and stress models are used within commercial casting simulation software to predict shrinkage porosity and hot tears. The simulations are validated through comparisons with observations made on experimental castings. Generally good agreement is obtained between the measured and predicted defect locations and extents. Design and process changes are introduced to mitigate the shrinkage and hot tear problems in these castings. The comparisons in the present study establish considerable confidence in the ability of casting simulation to predict shrinkage and hot tears in squeeze casting of magnesium alloys.

Introduction

Both shrinkage porosity and hot tears are common defects that occur during solidification of magnesium alloy castings. Shrinkage porosity forms when feeding flow becomes limited to a casting region containing liquid metal. Hot tears form when tensile strains create "volume deficits" in the mushy zone (semi-solid region). These volume deficits develop into hot tears if the local solid fraction is large enough that the deficits cannot be fed by the remaining liquid.

Predicting shrinkage porosity and hot tears with casting simulation software is a difficult task. Accurate prediction requires accurate modeling of casting solidification (including feeding flow velocities and shrinkage porosity formation), as well as accurate modeling of the evolution of stresses and strains throughout the solidifying casting. Two simulation models have recently been developed that can predict the relevant phenomena involved in shrinkage porosity formation and hot tearing. The first model is an advanced feeding model that predicts melt pressure, feeding flow, and shrinkage porosity formation and growth during casting solidification. This model solves a pressure equation that is derived by combining the multiphase mass and momentum conservation equations. During solidification, melt pressure and feeding velocity are calculated throughout the casting cavity. Shrinkage porosity forms in solidifying metal when the local melt pressure drops sufficiently low, and then this porosity grows until solidification is complete [1-2]. The second model is a viscoplastic deformation model that predicts stresses, strains, deformations and porous damage evolution during casting solidification and subsequent cooling. This model employs a viscoplastic constitutive model for the mushy zone. The total strain is taken as the sum of the thermal, elastic and viscoplastic strains. Porous damage is computed by integrating the volumetric portion of the viscoplastic strain rate over time, beginning when the feeding flow is cut off. Hot tears occur in regions containing porous damage [3-5]. Two recent studies have been performed utilizing the new viscoplastic strain model; one study successfully

predicted hot tears in simple experimental AZ91D castings [3], and the other study used forces measured during binary Mg-Al alloy solidification to calibrate mechanical properties of magnesium alloys [5]. Due to space limitations, these new models are not presented here; see Refs. [1-5] for model descriptions and details. The present investigation focuses on the application of these models, utilizing them to simulate squeeze cast magnesium alloy control arms.

Control Arm Casting Trials

This study considers two preliminary designs of a magnesium alloy control arm (see Fig. 1). These control arms were produced as squeeze castings, using the steel die depicted in Fig. 2. Squeeze casting employs quiescent, laminar filling through a relatively thick ingate. High pressurization (up to 950 bar in the present process) is applied to the solidifying casting after filling is
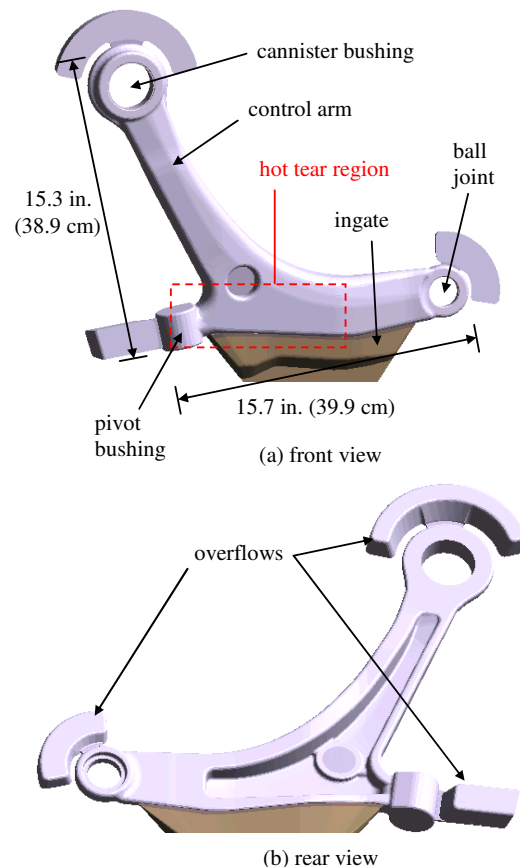

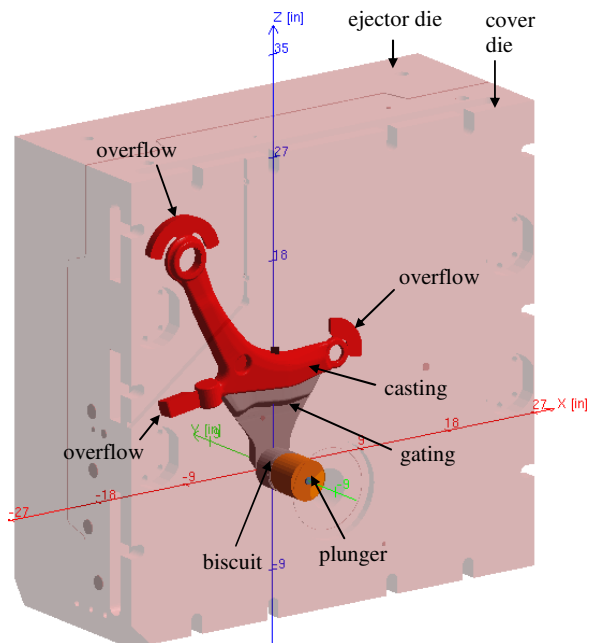Figure 1. Original AM60B control arm geometry.

Figure 2. Schematic of the control arm die arrangement.

Figure 4. Revised AZ91D control arm geometry.

heating and cooling line temperatures, the die preheat, the metal temperature at injection, the pressurization schedule and the casting cycle time line (Fig. 3) all remained the same as for the AM60B control arms. The primary goal of the casting re-design was achieved: hot tears did not occur in the revised AZ91D control arms. Some shrinkage porosity was still evident in the AZ91D control arms, but to a lesser extent than in the AM60B control arms.

Simulation Properties and Settings

The solidification path and thermophysical property data required to simulate casting solidification and cooling for AM60B and AZ91D were computed with the thermodynamic simulation software package JMatPro [6]. The mechanical properties required to perform the stress simulations for these alloys were determined as described in Refs. [3-5]. The control arm castings were simulated using the new advanced feeding and viscoplastic deformation models described in the introduction. Both of these new models have been implemented as special models within the commercial casting simulation software package MAGMAsoft [7]. The simulation parameters for both the original AM60B and the revised AZ91D castings were identical, except for the control arm geometry and the magnesium alloy utilized. The die set-up utilized for the simulations is shown in Fig. 2, and the casting cycle time line is given in Fig. 3. Automatic grid generation was used, resulting in about 400,000 computational cells in the casting cavities of the die. The die was modeled with the STEEL database provided in MAGMA. The metal injection temperature was set to 665°C for both alloys. The cooling and heating lines were all set to the reported temperatures used in the casting trials (the same values were used for both alloys). The casting/die interfacial heat transfer coefficient (IHTC) for each alloy was modeled with temperature-dependent curves provided in the MAGMA database, namely AM60B-HPDC and AZ91-HPDC. The casting/die contact boundary conditions necessary for stress calculations were defined such that the steel die was completely rigid, and the casting was deformable. Nine warm-up cycles were simulated to reach a relatively steady-state, and then the tenth cycle was simulated for the present analysis, utilizing the new advanced feeding and viscoplastic deformation models.

complete, and this pressure is maintained until shortly before the die is opened. The original control arm design, shown schematically in Fig. 1, was cast in AM60B. The metal was injected at 665°C. A series of heating and cooling lines were placed near the casting cavity in the die, kept at various temperatures selected to promote die temperatures near the casting surface that were favorable for producing sound castings. The time line for the casting cycle is given in Fig. 3. The castings produced with this process had excessive shrinkage porosity in a few locations, most notably in the pivot bushing of the control arm (see Fig. 1), because this was a hot spot in the casting. In addition, the castings were prone to hot tears near the ingate connection at the bottom of the control arm (see Fig. 1). Images of the radiographs showing porosity and photographs of the hot tears will be presented later, in comparison with simulation results.

In an effort to remedy the defects resulting from the original design, the casting process was revised. The alloy was changed to AZ91D, and the control arm casting geometry was slightly modified as shown in Fig. 4. The control arm pivot bushing was made hollow, in order to remove the hot spot. Also, the ribs on the back of the control arm were re-designed for structural and process optimization. The new AZ91D control arm design was cast using the same squeeze process as the original design; the
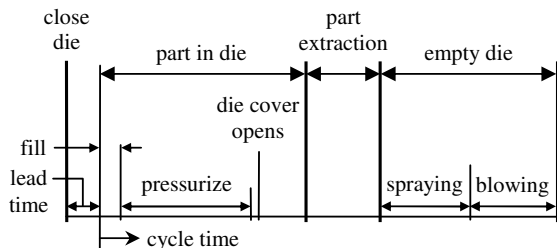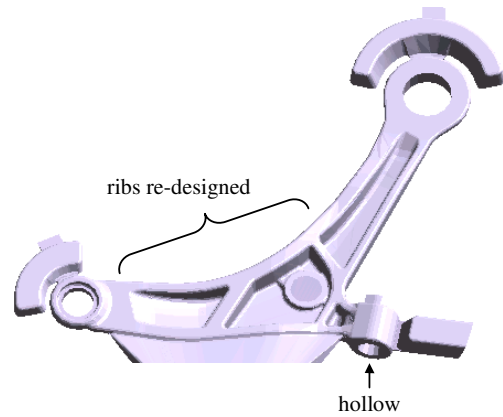

Figure 3. Casting cycle time line for the control arm.

Representative Simulation Results

An example of the melt pressure predicted during solidification for the AM60B control arm is shown in Fig. 5. The melt pressure contours (Fig. 5a) and liquid fraction contours (Fig. 5b) are shown 5.1 s into the cycle, during pressurization. Note that because the advanced feeding algorithm calculates the melt pressure, the squeeze casting pressurization (950 bar) is taken into account. Fig. 5b shows that the liquid fraction in the part of the control arm leading to the top ring is low (less than 30%). Feed metal moving up the control arm toward the top ring through partially solidified metal results in a large pressure drop from the pressurized value of 950 bar near the biscuit. Fig. 5b indicates two hot spots in the AM60B control arm; one in the pivot bushing and one just below the top ring of the control arm. Shrinkage porosity is expected to form in these locations because substantial liquid metal remains after feeding becomes difficult, which results in the melt pressure
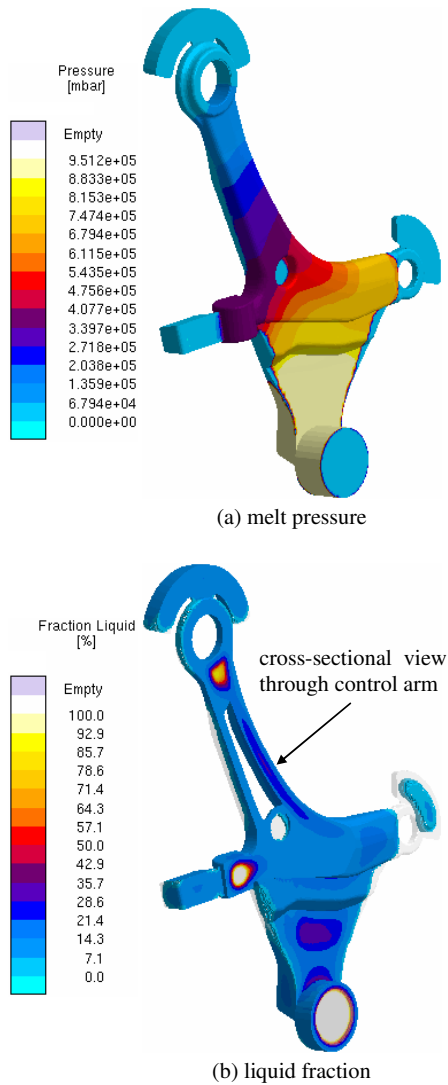
dropping low enough for porosity to form. The more liquid metal that is present when porosity forms, the more porosity will form to feed the remaining local solidification shrinkage.

Fig. 6 shows simulated feeding velocity results 2.9 s into the cycle, at a cross-section of the AM60B control arm near the top ring. Fig. 6a shows the liquid fraction contours at this time, and Fig. 6b shows velocity contours and vectors. The vector length indicates the relative magnitude of the velocity, as does the contour color scale. At the bottom right of Fig. 6b, feeding flow is seen moving up the control arm, through a channel in the arm with a high liquid fraction (see Fig. 6a). The velocity decreases once the feed metal reaches the hot spot because there is more high-liquid-fraction space in which the feed metal can move. As the feed metal flows into the upper ring, the feed metal velocity increases once again because of the small high-liquid-fraction channel that remains around the upper ring.

The final porosity predictions are given in Fig. 7a for the AM60B control arm, and in Fig. 7b for the AZ91D control arm. Fig. 7 shows a cross-sectional view that cuts through the upper part of

(a) melt pressure

(b) liquid fraction

Figure 5. Contours showing (a) melt pressure and (b) liquid fraction during pressurization of the AM60B control arm casting.
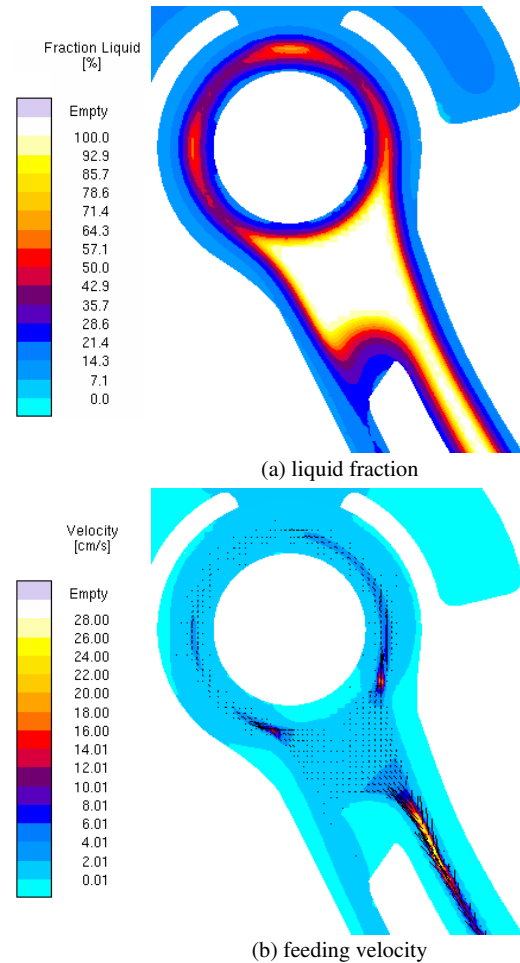

(a) liquid fraction

(b) feeding velocity

Figure 6. Contours showing (a) liquid fraction and (b) feeding flow velocity at a cross-section near the top of the AM60B control arm during solidification.

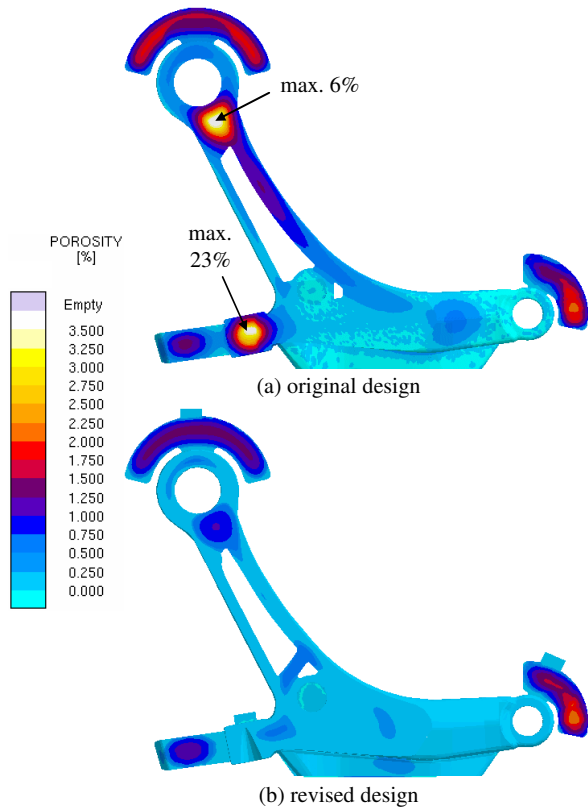(a) original design

(b) revised design

Figure 7. Predicted shrinkage porosity contours shown at a cross-section that reveals internal porosity for (a) original AM60B control arm design, and (b) revised AZ91D design.

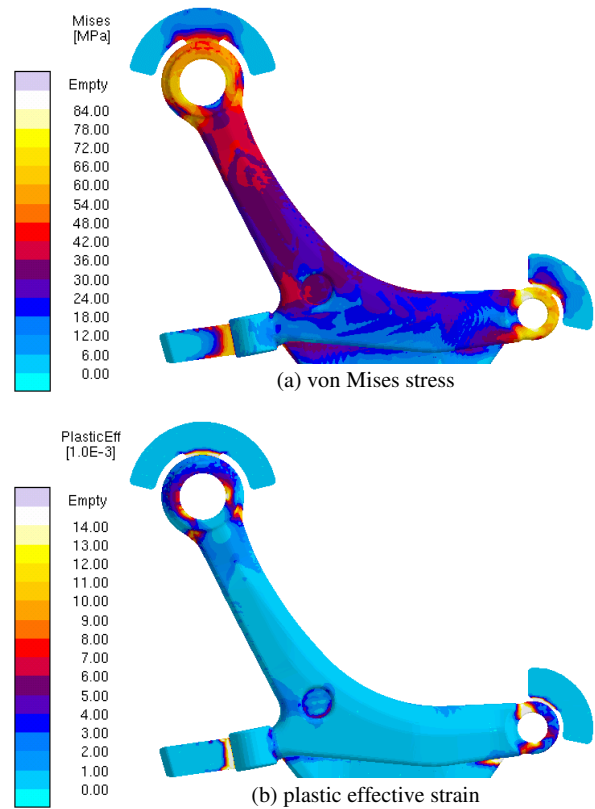(a) von Mises stress

(b) plastic effective strain

Figure 8. Simulated (a) von Mises stress and (b) plastic effective strain results for the AM60B control arm 20 s into the casting cycle, immediately prior to ejection from the die.

the control arms, showing the porosity in the two hot spots in the AM60B castings mentioned above; the control arms were not oriented in the simulation in a way that allows results to be shown on the casting mid-plane, which would be optimal. However, the mid-plane (i.e., maximum) porosity contour plots in each region of interest in both control arms are provided later, when the simulated porosity is compared to radiographs. Fig. 7a shows that, as expected, the two hot spots in the AM60B casting contain significant amounts of shrinkage porosity. In addition, smaller amounts of porosity are predicted in the upper part of the control arm below the hot spot. Comparing the revised AZ91D control arm porosity prediction in Fig. 7b to the AM60B prediction in Fig. 7a, it is clear that changing from AM60B to AZ91D and modifying the geometry significantly reduces the amount of shrinkage porosity predicted. The porosity in the hot spot near the upper ring is less severe in Fig. 7b than in Fig. 7a, and the porosity in the arm directly below this hot spot is significantly reduced as well. Also, hollowing out the pivot bushing in the revised geometry has alleviated the large porosity indication in that location.

Sample stress-strain results are provided for the AM60B control arm in Fig. 8. These results are shown immediately prior to the part being ejected from the die. Fig. 8a shows the von Mises stress in the control arm, and Fig. 8b shows the plastic effective strain. The control arm is completely solidified at this time. The stresses seen in Fig. 8a are an instantaneous result; the high stress regions around the rings (i.e., the cannister bushing and ball joint) are due

to the rings straining against the rigid die, which is preventing the control arm from freely contracting as it cools. On the other hand, the plastic strains in Fig. 8b are a cumulative result, because of the plastic (irreversible) nature of the strain.

The final damage and distortion predictions for the control arms are given in Fig. 9. The magnitude of the porous damage scale is not important; only the relative amounts of damage are relevant. The AM60B control arm prediction is given in Fig. 9a. The shadow shows the original control arm shape, and the distortion is magnified by a factor of twenty to make it more noticeable. Note the distortion around the two rings, where the die prevented the casting from freely contracting as it solidified and cooled. The contour colors indicate the predicted level of porous damage. The highest damage predictions shown in Fig. 9a occur around the pivot bushing. Smaller amounts of damage are predicted just below the top ring of the control arm, and along the junction between the bottom of the control arm and the ingate; the latter indication is difficult to see in this view, but it will be shown more clearly when the simulated porous damage results are compared to the experimental hot tear pictures. Fig. 9b shows the final distortion and damage prediction for the AZ91D control arm. No significant damage is predicted in the revised control arm, which agrees with the finding that hot tears did not occur in the AZ91D control arms. Comparing Figs. 9a and 9b, it is also evident that the AZ91D control arm undergoes significantly less distortion than the AM60B control arm.
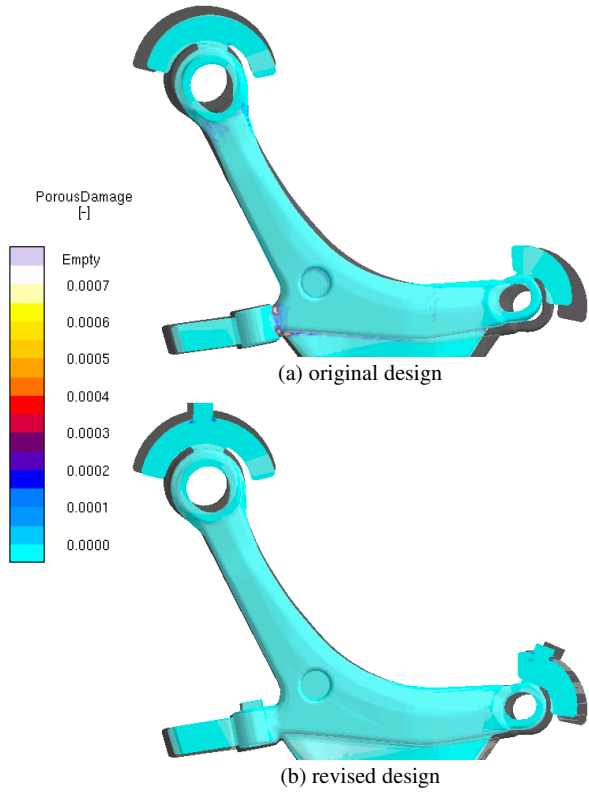
96

(a) original design

(b) revised design

Figure 9. Predicted distortion and damage at end of casting cycle, for (a) original AM60B design, and (b) revised AZ91D design. Contours show porous damage, with the shape indicating distortion (magnified 20x, original shape shown as a shadow).

As explained in the introduction, porous damage is determined by integrating the volumetric portion of the plastic strain rate over time, beginning when feeding flow is cut off. This can be understood by considering the AM60B simulation results. For example, high strain is seen around the lower right ring in Fig. 8b. However, the porous damage result in Fig. 9a indicates that no damage is evident near this ring. This can be explained by considering Fig. 7a, which shows that almost no shrinkage porosity forms in this region, indicating that it is well-fed until solidification is complete. So although the strain in the area is high, no porous damage forms because the region is well fed throughout solidification. Another example is the region where the pivot bushing connects to the control arm. Fig. 8b shows elevated strain indications in this region. Furthermore, Fig. 7a shows that this location contains a significant amount of shrinkage porosity, indicating that there was a substantial amount of liquid remaining in the pivot bushing when feeding was cut off (as shown in Fig. 5b). Therefore, shrinkage porosity was readily available in this region for tensile strains to stretch and enlarge, creating the predicted porous damage.

Comparison with Casting Results

The simulated AM60B porosity results are compared to radiographs and micrographs of these control arm castings in Fig. 10. The micrographs in the top row of Fig. 10 illustrate the dendritic nature of the porosity (with the possible exception of region 4), indicating that it is indeed solidification shrinkage seen in the radiographs. Regions 1 and 2, where hot spots are located in the casting, show good agreement between experiment and simulation; porosity is predicted where visible indications are seen in the radiographs of these regions. The radiograph of region 3 shows very minor indications, observed better in the micrograph above the region 3 radiograph. Correspondingly, small amounts of porosity (0.25 – 0.5%) are predicted in that region. The
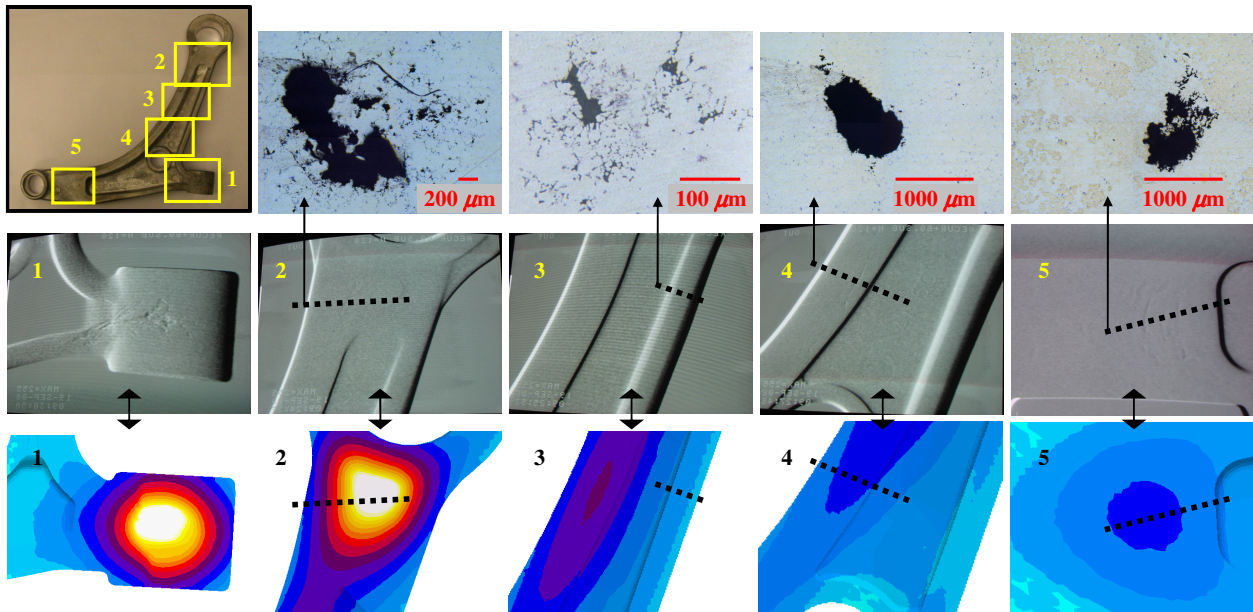

Figure 10. Comparison between AM60B control arm radiographs (middle row) and simulated porosity contour cross-sections (bottom row) at five locations indicated on the upper left photograph. The reminder of the top row contains micrographs at the locations indicated by the dotted lines. The porosity scale, given in Fig. 7, ranges from 0 – 3.5%.

radiographs and micrographs for regions 4 and 5 also show evidence of porosity, and the simulation results for those regions have porosity predictions of 0.75 – 1%. Overall, Fig. 10 shows excellent agreement between regions where porosity is predicted and visible radiographic shrinkage indications.

Similarly, the AZ91D porosity simulation results are compared to casting radiographs in Fig. 11. Circles encompass visible porosity in the radiographs. The top row of this figure compares simulated and measured shrinkage in region 1, the upper portion of the control arm (see the schematic at the upper left of Fig. 11). The simulation predicts small amounts of porosity (note the porosity scale at the upper right of the figure) in the hot spot and circumferentially in the top half of the ring in this region, and the radiographs show shrinkage indications in these areas as well. Region 2, containing the pivot bushing, is compared in the
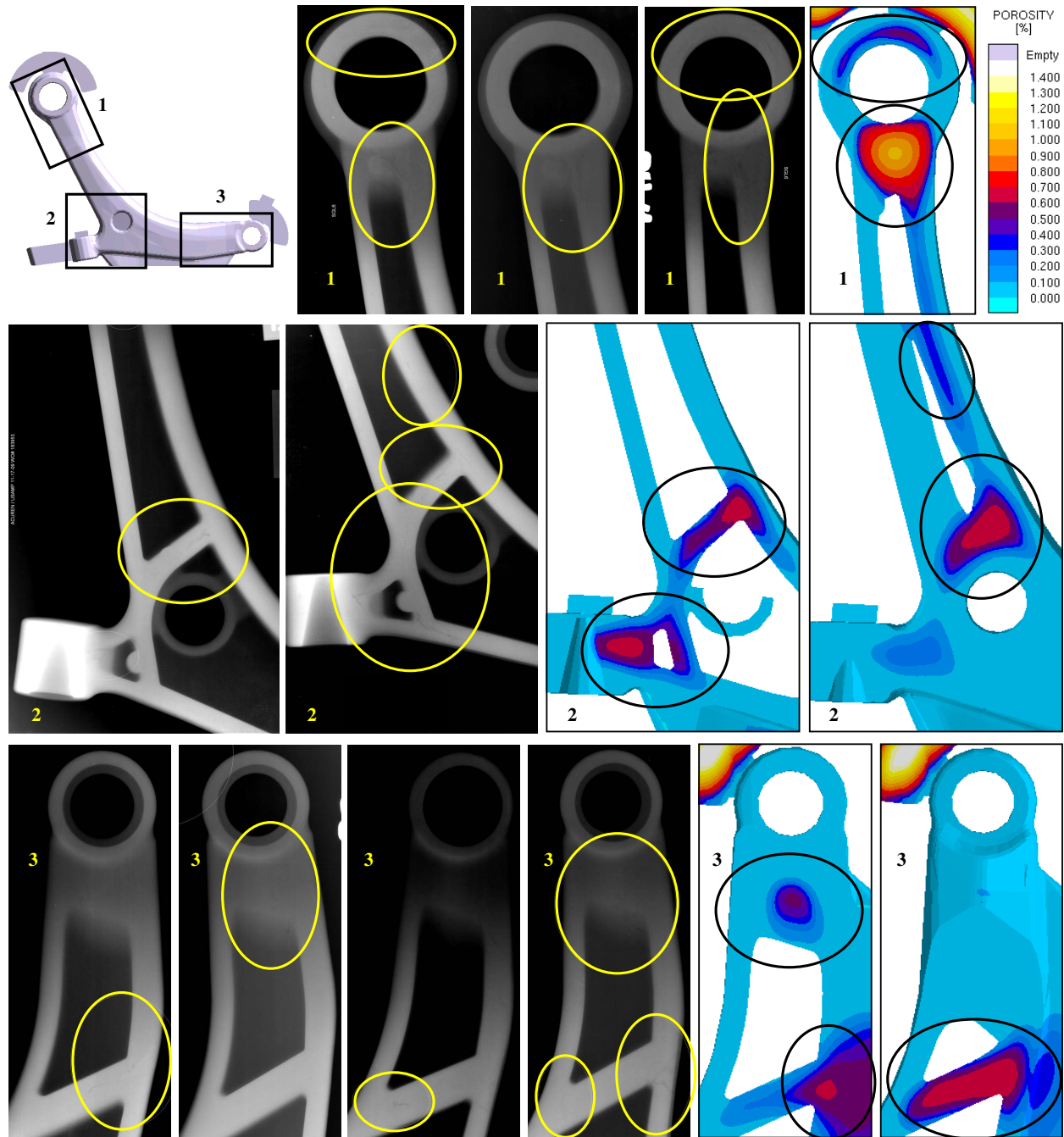

Figure 11. Comparison between radiographs and simulated porosity contours for the revised AZ91D control arm at three locations (one location per row), with locations indicated on the upper left schematic of the control arm. The porosity scale is given in the upper right.

middle row. Two simulated cross-sections are shown because a single cross-section does not characterize all the porosity. Again, excellent agreement is found between porosity visible in the radiographs in the ribs and near the pivot bushing, and regions where porosity is predicted in the simulation. Finally, region 3, containing the other ring, is compared in the bottom row (rotated 90° counterclockwise). Again, two simulation cross-sections are given to show all the relevant porosity. Once more, the locations near the ring and in the ribs, where indications are visible on the radiographs, are in excellent agreement with the regions where porosity is predicted in the simulation. In summary, both the AM60B and the AZ91D porosity predictions show excellent qualitative agreement with the locations of visible shrinkage shown in the radiographs and micrographs of the experimental castings.

Figs. 12 and 13 provide a comparison between the hot tears observed in the AM60B control arm castings (see Fig. 1 for location) and the simulated damage for these castings. Fig. 12a is a photograph of a hot tear that runs along the junction between the control arm and the ingate (indicated by a dotted line), and Fig. 12b shows the damage prediction in this region. Some degree of damage is predicted all along the length of the hot tear in the photograph. Fig. 13 focuses on the region where the pivot bushing connects to the control arm (i.e., left side of Fig. 12a). The photograph in the upper left indicates four regions where additional hot tear pictures are shown. The pictures from all four of these regions show evidence of hot tearing, and the simulation predicts relatively high porous damage in all of these regions.

The simulated damage prediction for the AM60B control arms did produce one false positive result. A small spot of relatively high damage was predicted on the bottom of the control arm, on the far right edge of the ingate where it meets the control arm; the location corresponds to the region of high plastic strain at the
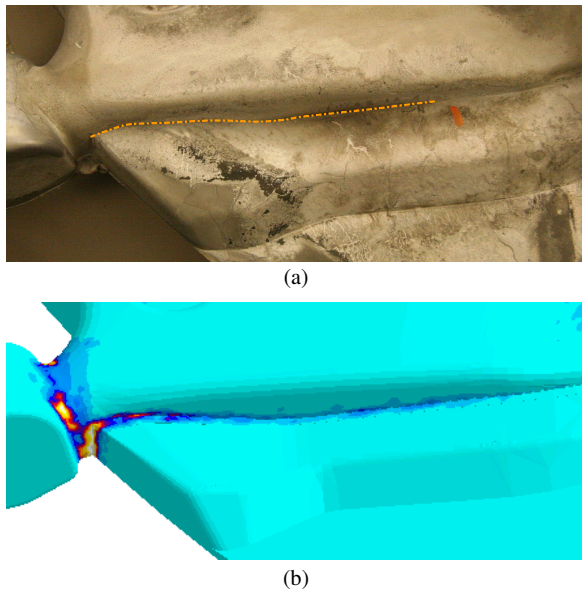

(a)

(b)

Figure 12. Comparison between (a) experimental AM60B casting hot-tear (indicated by dotted line), and (b) simulated porous damage. The porous damage scale is given in Fig. 9.
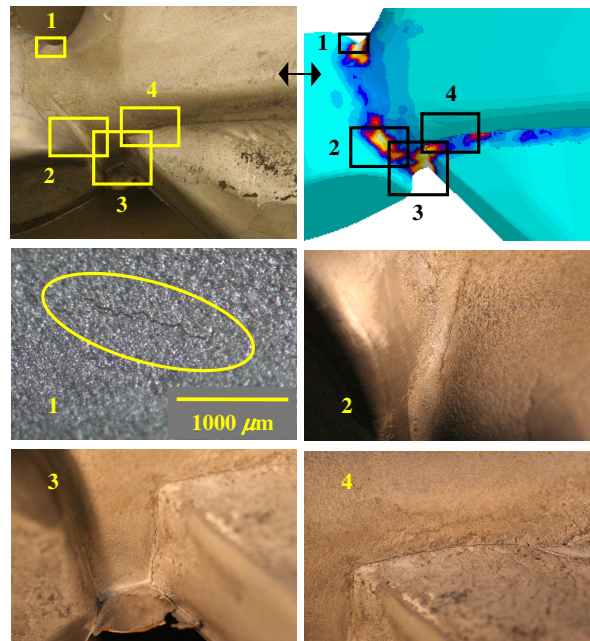

Figure 13. Further comparison between experimental AM60B casting hot-tears and simulated porous damage (top row), along with four close-up pictures showing hot tearing. The porous damage scale is given in Fig. 9.

top right corner of the ingate in Fig. 8b. Because the damage indication is on the bottom surface of the control arm, this spot is not visible in Fig. 9a. Although damage was predicted here, no hot tearing was seen in this region. However, aside from this, the correlation between locations with predicted damage and the occurrence of hot tears in both the AM60B and the AZ91D control arm castings is excellent. In general, porous damage predictions indicate potential initiation sites for hot tears. The results for the AM60B casting imply that the tears likely initiated near the pivot bushing, where the highest damage is predicted.

Conclusions

An experimental study was performed involving two preliminary designs of squeeze cast magnesium alloy control arms. The first design utilized AM60B, and resulted in control arms with significant porosity and hot tears. After this, the geometry was re-designed and the alloy was changed to AZ91D. Control arms cast with these revisions exhibited much less shrinkage porosity, and did not show evidence of hot tears. The casting of both designs was simulated using a new advanced feeding model and a new viscoplastic deformation model. For both the AM60B and AZ91D control arms, excellent agreement was seen between regions where porosity was predicted and where visible shrinkage was seen on radiographs, as well as between regions where porous damage was predicted and regions containing hot tears. The excellent qualitative agreement observed in both the porosity and hot tear predictions indicates that both new models are useful predictive tools for the squeeze casting process used to produce these castings.

References

1. K.D. Carlson, Z. Lin, R.A. Hardin, C. Beckermann, G. Mazurkevich, and M.C. Schneider, "Modeling of Porosity Formation and Feeding Flow in Steel Casting," *Modeling of Casting, Welding and Advanced Solidification Processes - X*, ed. D.M. Stefanescu et al., (Warrendale, PA: TMS, 2003), pp. 295-302.
2. K.D. Carlson, Z. Lin and C. Beckermann, "Modeling the Effect of Finite-Rate Hydrogen Diffusion on Porosity Formation in Aluminum Alloys," *Metall. Mater. Trans. B*, 36B (2007), pp. 541-555.
3. M.G. Pokorny, C.A. Monroe, C. Beckermann, L. Bichler, and C. Ravindran, "Prediction of Hot Tear Formation in a Mg Alloy Permanent Mold Casting," *Int. J. Metalcasting*, 2 (2008), pp. 41-53.
4. C.A. Monroe, C. Beckermann, and J. Klinkhammer, "Simulation of Deformation and Hot Tears Using a Visco-Plastic Model with Damage," *Modeling of Casting, Welding, and Advanced Solidification Processes - XII*, ed. S.L. Cockcroft and D.M. Maijer (Warrendale, PA: TMS, 2009) pp. 313-320.
5. M.G. Pokorny, C.A. Monroe, C. Beckermann, Z. Zhen, and N. Hort, "Simulation of Stresses During Casting of Binary Magnesium-Aluminum Alloys," *Metall. Mater. Trans. A*, (in press, 2010).
6. JMatPro v.4.0, Sente Software Ltd., Surrey Technology Centre, Surrey GU2 7YG, United Kingdom.
7. MAGMAsoft v4.5, Magma GmbH, Aachen, Germany.